

EXPERIMENTAL INVESTIGATION ON THE INNER DUCT SURFACE UNSTEADY PRESSURE OF A DUCTED PROPELLER

Jingang Li[1], Yendrew Yauwenas[1], Danielle Moreau[1] & Con Doolan[1]

[1]University of New South Wales, Sydney, NSW, 2052, Australia

Abstract

This study experimentally investigates the unsteady wall-pressure fluctuations on the inner duct wall generated by a low-speed ducted propeller using the remote microphone method. Measurements were conducted in the UNSW Anechoic Wind Tunnel under hover flight conditions using a circular duct with multiple axial propeller positions. A finite-length joint duct model was developed to predict the wall-pressure response by incorporating acoustic reflections and transmission between connected duct sections of varying radius. The model was first validated using a pseudo-monopole source inside the duct. The predicted overall sound pressure level (OASPL) distributions showed good agreement with the measurements and reproduced the principal axial variation of the wall-pressure field. The ducted propeller measurements showed that the wall-pressure spectra were dominated by tonal components at the blade-passing frequency and its harmonics. The tonal OASPL distributions exhibited peak amplitudes near the propeller plane and decayed with increasing axial distance. The model captured the dominant tonal peaks and the overall axial trends of the measured wall-pressure distributions, although discrepancies in amplitude were observed due to wake–boundary-layer interaction and limitations in the reconstructed dipole-force spectrum. The results provide insight into the interior acoustic behavior of ducted propellers and the influence of duct geometry and propeller position on unsteady wall-pressure fluctuations.

Keywords: aeroacoustics, ducted propeller, unsteady wall pressure

1. Introduction

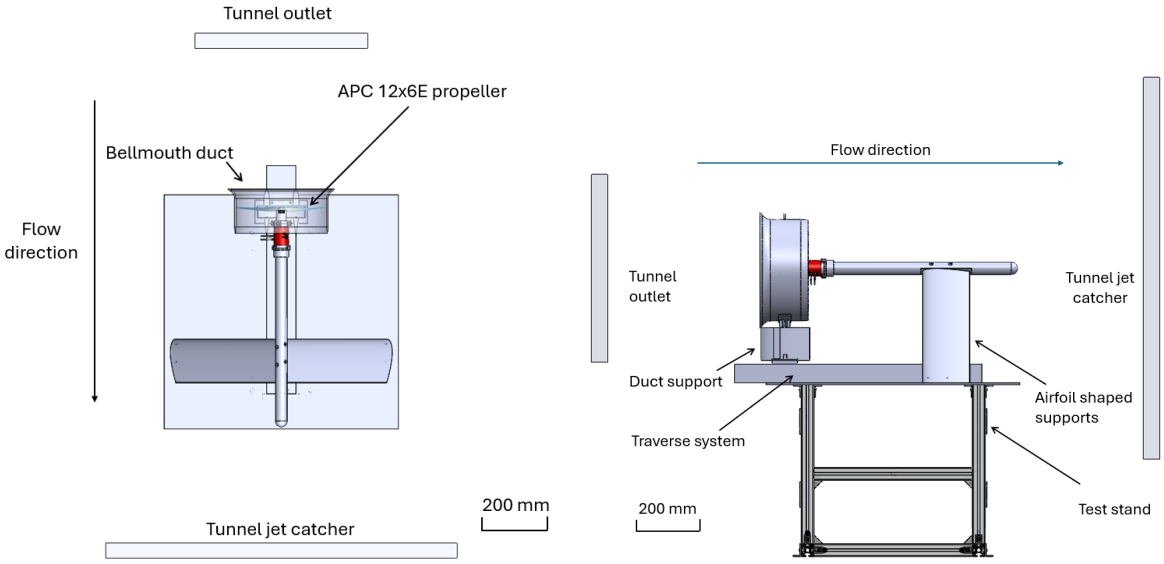
Unmanned aerial vehicles (UAVs) have attracted sustained research interest due to their versatility and wide range of applications in both civilian and military domains [1]. Ducted propeller configurations are commonly adopted to enhance thrust and propulsive efficiency, and are particularly advantageous for electrically powered UAVs, whose endurance is constrained by battery capacity [2]. However, the presence of a rotating noise source within a short annular duct gives rise to a complex internal pressure field, leading to radiated far-field noise that remains challenging to predict accurately [3]. Accordingly, the present study aims to experimentally characterize the unsteady wall pressure on the inner duct wall generated by a low-speed propeller operating within a circular duct using the remote microphone method. Particular emphasis is placed on the influence of propeller axial position on the resulting pressure fluctuations.

2. Methodology

2.1 Experimental Setup

Unsteady pressure fluctuations on the inner duct surface of a ducted propeller were measured in the UNSW Anechoic Wind Tunnel [4] using the test rig shown in Figure 1, under hover flight conditions. A two-bladed APC 12×6E propeller (12-inch diameter, 6-inch pitch) was driven by a SunnySky X2820 brushless DC motor powered by a 4S LiPo battery. The motor speed was regulated using a

Turnigy Super Brain 60 A electronic speed controller with feedback provided by a Monarch Instrument ROLS-P laser tachometer, enabling closed-loop rotational-speed control. The propeller speed was maintained at 5400 RPM for all test cases, corresponding to a blade-passing frequency (BPF) of 180 Hz.



(a) Top view (b) Side view

Figure 1 – Schematics of the experimental configuration.

The duct used in the experiments is shown in Figure 2. The duct length L is equal to $50\%D$, which is expressed as a percentage of the propeller diameter D. The duct profile consists of a NACA 0018 airfoil section combined with a cylindrical segment. The airfoil was divided at its maximum thickness, with the forward and aft portions forming the leading- and trailing-edge sections of the duct, respectively. A smooth bellmouth inlet, defined by a circular arc, was employed to mitigate flow separation at the duct entrance. The complete geometry was obtained by revolving this composite profile about the propeller axis. The duct wall thickness was 5 mm, and the inner radius, a, was 155 mm, yielding a tip clearance of 2.6 mm ($0.85\%D$) within the cylindrical duct section.
Five axial propeller positions were examined during the tests, which are defined relative to the duct center and expressed as percentages of L: $+50\%L$, $+25\%L$, $+0\%L$, $-25\%L$, and $-50\%L$, as illustrated in Figure 2.

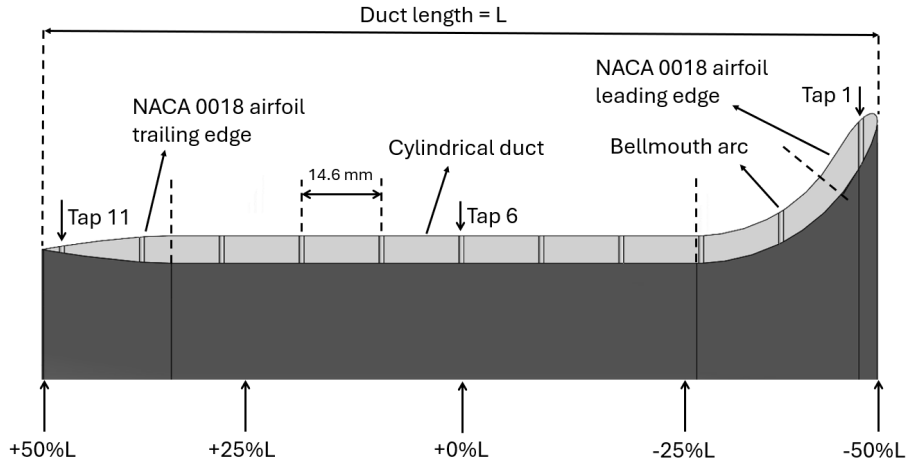


Figure 2 – The cross section of the $50\%D$ duct and the pressure tap locations on the inner duct surface.

The remote microphone method was used to measure unsteady wall-pressure fluctuations. The ar-

rangement of 11 equi-spaced pressure taps along the duct is shown in Figure 2. Pressure signals from each tap were transmitted through flexible tubing to a GRAS 1/4-inch Type 40PH free-field microphone housed in a protective enclosure. The housing incorporated a 1.6 mm diameter channel with a T-junction that split the signal between the microphone and a 3 m anechoic termination, following the configuration of Awasthi et al. [5].

The GRAS Type 40PH microphone provides a flat frequency response (± 2 dB) up to approximately 15 kHz. The microphone signals were acquired using a National Instruments PXI data acquisition system at a sampling rate of 65.5 kHz over a duration of 32 s.

Microphone calibration was performed using the cavity-calibration method [5], as shown in Figure 3. A calibration coupler housing both a speaker (source) and a factory-calibrated reference microphone, oriented perpendicular to each other, was mounted over each pressure tap. This arrangement ensured that both the remote and reference microphones were exposed to the same acoustic field. The input voltage to the speaker, along with the responses of the reference and remote microphones, were recorded simultaneously. The complex transfer function of the measurement system is given by

$$H_{cal}(f) = \frac{\Phi_{SM}(f)}{\Phi_{SR}(f)} \tag{1}$$

where f is the frequency, $\Phi_{SM}(f)$ is the cross-spectrum between the speaker input signal and the remote microphone output, and $\Phi_{SR}(f)$ is the cross-spectrum between the speaker input signal and the reference microphone output.

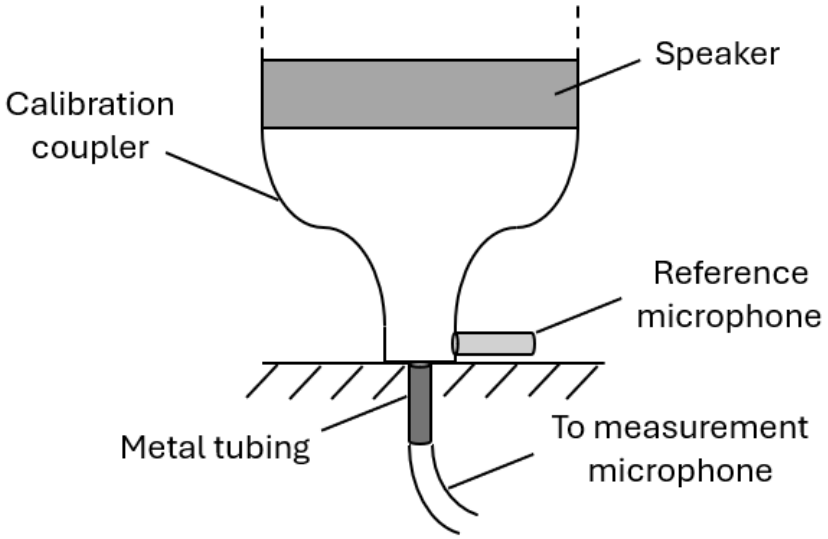


Figure 3 – The remote microphone calibration setup.

2.2 Joint Duct Model

To aid the interpretation of the experimental results presented in the following section, an analytical model is introduced to predict the unsteady wall pressure of a ducted propeller with axially varying duct radius, which builds on the finite duct model of Tomko [3]. For an infinite duct, the acoustic pressure generated by the propeller, which can be modeled as a dipole ring, is expressed as

$$p(x,r,\theta,\omega) = \sum_{m=-\infty}^{\infty} F_m(\omega) T_{rotor,m} \tag{2}$$

where $F_m(\omega)$ is the amplitude of the propeller thrust force for mode m, and $T_{rotor,m}$ is the corresponding rotor transfer function, which is given by

$$T_{rotor,m} = \sum_{n=1}^{\infty} \varepsilon \frac{J_m(k_{mn}r)J_m(k_{mn}r_0)}{\sigma_{mn}} \pi e^{ik_{z,mn}|x-x_0|} \left((-1)^b r_0 \cos\varphi - \frac{m}{k_{z,mn}\sin\varphi} \right) \tag{3}$$

where $\varepsilon = 0.5$ for $m = 0$ and $\varepsilon = 1$ otherwise. The term J_m denotes the Bessel function of the first kind, and (x, r) and (x_0, r_0) are the axial and radial coordinates of the observer and source, respectively. The radial modal wavenumber k_{mn} satisfies the hard-wall boundary condition $J'_m(k_{mn}r) = 0$ at $r = a$, and $k_{z,mn}$ is the axial modal wavenumber. The blade stagger angle is denoted by φ. The parameter b is defined as $b = 0$ for $x \geq x_0$ and $b = 1$ otherwise. For $m = 0$, an additional plane-wave term, $\frac{e^{ik|x-x_0|}}{a^2}(-1)^b r_0 \cos\varphi$, must be added outside the summation. The normalization factor σ_{mn} is given by

$$\sigma_{mn} = \pi a^2 \left(1 - \frac{m^2}{k_{mn}^2 a^2}\right) J_m^2(k_{z,mn}) \tag{4}$$

For a finite-length duct, acoustic waves are partially reflected at each open end. These reflections give rise to an infinite sequence of waves propagating back and forth within the duct. This behavior can be represented using the method of image sources, as illustrated in Figure 4, where each reflection is modeled as a virtual source located symmetrically about the duct termination.

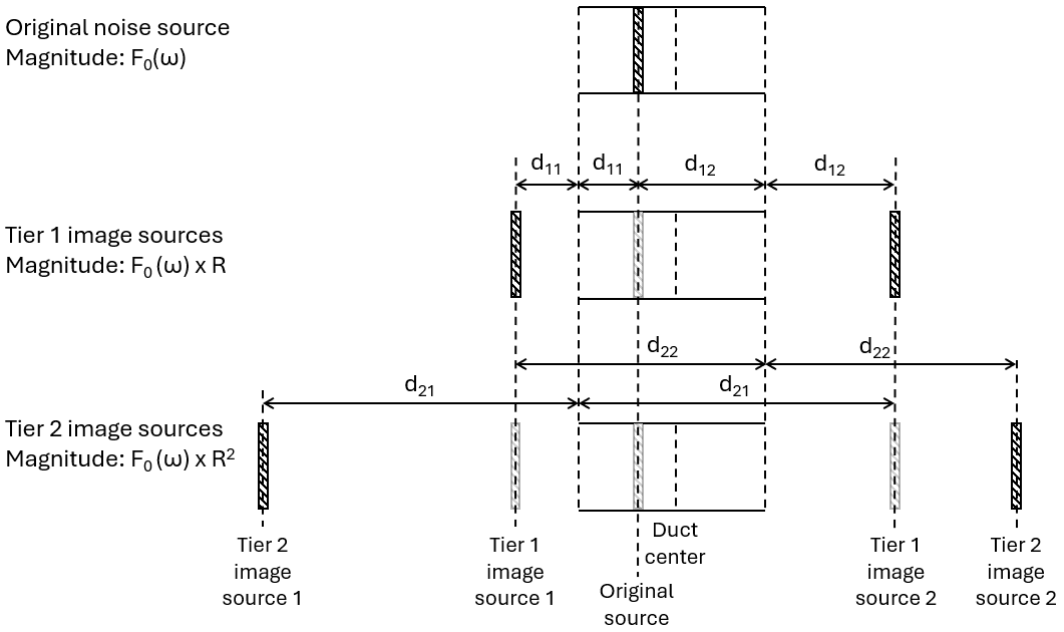


Figure 4 – Schematic of two tiers of image noise sources result from a finite length duct. $F(\omega)$ is the force amplitude of the original source, and R is the reflection coefficient at the duct end.

The amplitude of an image source of tier n (i.e., after n reflections) is given by $F_0(\omega)R^n$, where $F_0(\omega)$ is the source amplitude and R is the reflection coefficient at the duct termination. In the present study, $R = 0.6$ is adopted following Levine and Schwinger [6]. The wall pressure in a finite duct is then approximated by superposing the contributions from the primary source and all image sources within the infinite-duct formulation.

The above formulation is restricted to ducts of uniform cross-section. To account for the bellmouth geometry, the duct shown in Figure 2 is modelled as two connected finite ducts with different radii, representing the cylindrical and bellmouth sections, respectively (Figure 5). The dashed lines indicate discrete stations: station 0 corresponds to the source plane, station 1 to the junction between the two sections, and stations 2 and 3 to the open ends.

As an incident acoustic wave P_{in} traverses the junction (station 1), it undergoes partial reflection (P_R) and transmission (P_T). The corresponding reflection and transmission coefficients are determined by the cross-sectional areas of the adjoining sections [7]:

$$R = \frac{S_1 - S_2}{S_1 + S_2} \tag{5}$$

$$T = \frac{2S_1}{S_1 + S_2} \tag{6}$$

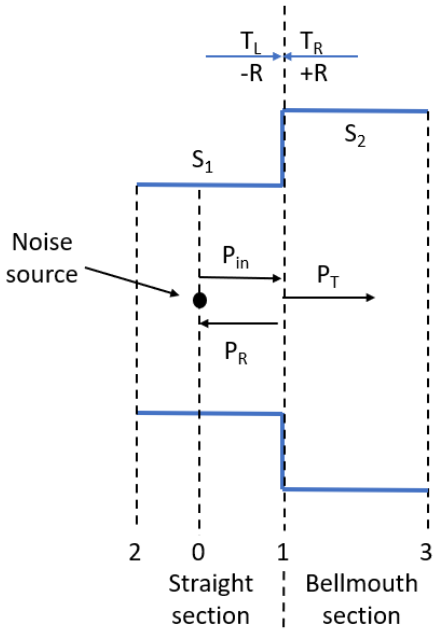


Figure 5 – Schematic of the modified finite duct model consists of two duct segments.

where S_1 and S_2 are the upstream and downstream cross-sectional areas, respectively.
When applying the image-source method to the joint duct, the propagation and reflection paths depend on the sequence of interactions with the junction and duct terminations, resulting in unique image-source locations for each path. For instance, for waves undergoing two reflections, a wave reflected first at the junction (station 1) and then at an open end (station 2 or 3) propagates through both duct sections. In contrast, a wave reflected first at an open end and subsequently at the junction may only propagate within one section before radiating into the far field. These differing reflection pathways must be accounted for when assembling the total wall-pressure response.

3. Results

3.1 Monopole Source Test

A pseudo-monopole source was employed to validate the joint duct model prior to the propeller experiments. The source was implemented by placing the remote microphone calibration coupler (Figure 3) inside the duct, with its outlet axially aligned with the fifth pressure tap.
For a monopole source of strength q_0 within an infinite, hard-walled cylindrical duct, the acoustic pressure field $P(\mathbf{x},\omega)$ is given by

$$P(\mathbf{x},\omega) = \int_V q_0 G_M(\mathbf{x},\mathbf{x_0};\omega) dV(\mathbf{x_0}) \tag{7}$$

where $\mathbf{x} = (r,\theta,x)$ and $\mathbf{x}0 = (r_0,\theta_0,x_0)$ denote the observer and source locations, respectively. The Green's function G_M is defined as:

$$G_M(\mathbf{x},\mathbf{x_0};\omega) = \frac{e^{ik|x-x_0|}}{2i\pi a^2 k} \sum_{m=0}^{\infty}\sum_{n=1}^{\infty} \varepsilon \frac{J_m(k_{mn}r)J_m(k_{mn}r_0)}{i\sigma_{mn}k_{z,mn}} \cos\left(m(\theta-\theta_0)\right) e^{ik_{z,mn}|x-x_0|} \tag{8}$$

The calibration coupler outlet is approximated as a cylindrical monopole source with base area S and height δ, such that Eq. (7) reduces to

$$P(\mathbf{x},\omega) = q_0 \delta S G_M(\mathbf{x},\mathbf{x_0};\omega) \tag{9}$$

The source strength q_0 is determined experimentally. The acoustic pressures measured by the reference microphone (P_{ref}) and a far-field microphone (P_{ff}) are used to define an empirical transfer function, H, according to

$$P_{ff} = P_{ref} H \tag{10}$$

P_{ff} can also be expressed using the free-field Green's function as:

$$P_{ff} = \frac{i\omega\rho Q_s e^{-ikr}}{4\pi r} \tag{11}$$

where ρ is the air density, Q_s is the monopole volume velocity, and r is the distance between the source and the far-field microphone.
Equating Eqs. (10) and (11) yields an expression for q_0:

$$q_0 = \frac{4\pi r P_{ref} H}{iSC_M e^{-ikr}} \tag{12}$$

where C_M is an empirical correction factor accounting for deviations of the calibration coupler from an ideal monopole source (taken as 0.1).
Substituting Eq. (12) into Eq. (9) gives

$$P(\mathbf{x},\omega) = \frac{4\pi r \delta P_{ref} H}{iC_M e^{-ikr}} G_M(\mathbf{x},\mathbf{x_0};\omega) \tag{13}$$

The overall sound pressure level (OASPL) between 100 and 4000 Hz is computed as

$$OASPL_i = 10\log_{10}\left(\frac{\int \mathrm{PSD}_i(f)df}{p_{\mathrm{ref}}^2}\right) \tag{14}$$

where $\mathrm{PSD}_i(f)$ is the power spectral density at the ith microphone, $df = 1$ Hz is the frequency resolution, and $p\mathrm{ref} = 20\,\mu\mathrm{Pa}$ is the reference pressure for air.

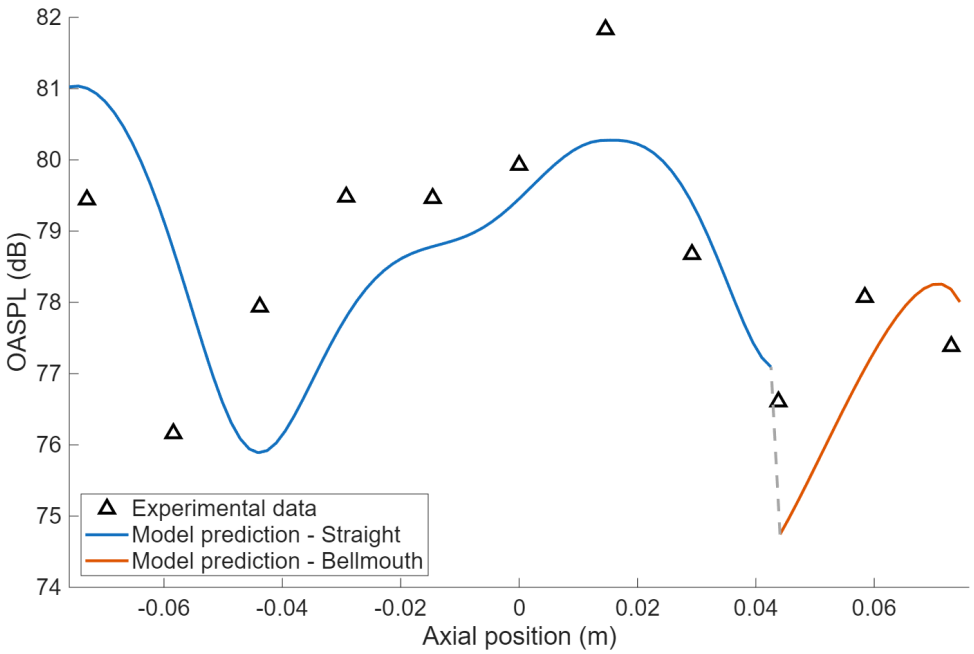


Figure 6 – Comparison of the measured and predicted unsteady duct wall pressure OASPL generated by a monopole source along the axial direction.

Figure 6 compares the measured and predicted OASPL distributions along the duct wall. The model captures the overall axial trend and relative variation in amplitude with good agreement. However, systematic axial offsets are observed, notably a forward shift of the valley near the tenth pressure tap (at -0.0584 m) and the peak near the second pressure tap (at 0.0584 m).
Inspection of Eqs. (8) and (13) shows that the axial dependence is governed primarily by the term $|x - x_0|$. To assess the sensitivity of the model to source location, OASPL distributions were computed for monopole sources at different axial positions. The results are shown in Figure 7.
As the source is shifted upstream, the primary peak translates in the same direction but with reduced sensitivity compared to downstream shifts. In contrast, the valley near the tenth microphone shifts

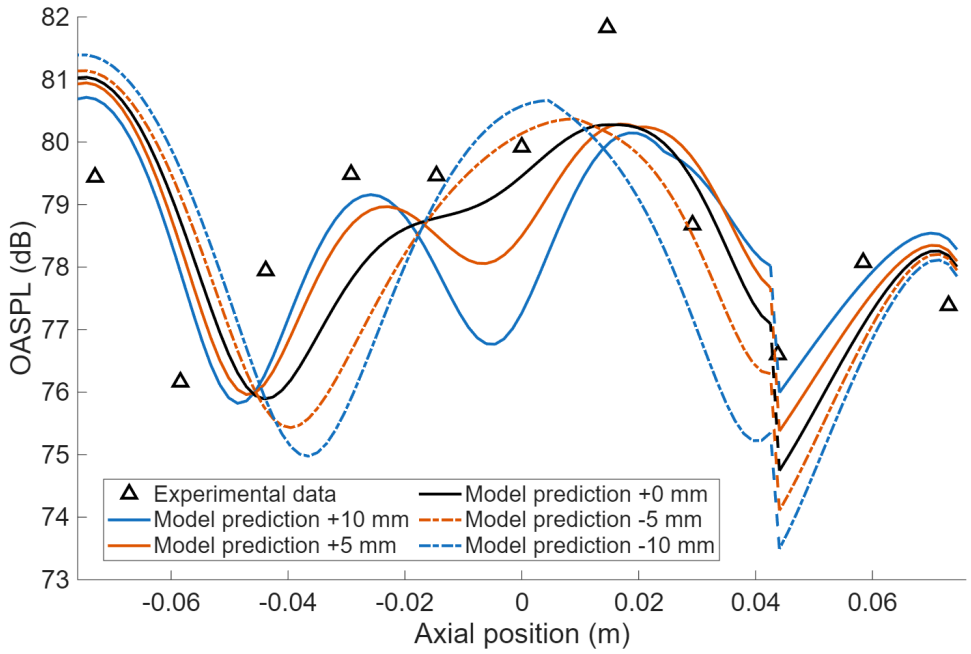


Figure 7 – Comparison of the model predicted unsteady duct wall pressure OASPL with different source axial positions.

in the opposite direction. The intermediate "plateau" region (pressure tap locations 6–8, between 0 and -0.0292 m) is modified in both shape and amplitude due to the interaction of these features. In the bellmouth section, the source position predominantly affects the overall amplitude, with higher OASPL observed for upstream source locations.

Given the spacing between adjacent pressure taps (14.6 mm) and the duct length (L=152 mm), the model demonstrates sufficient axial sensitivity for the present measurements. The remaining discrepancies between measured and predicted OASPL distributions are therefore attributed to modeling assumptions, most notably the use of constant reflection coefficients at the duct terminations.

3.2 Ducted Propeller Experiment

Ducted propeller measurements were conducted as described in Section 2.1. To obtain the modal dipole force spectrum, $F_m(\omega)$, required as input to the model, the iterative method developed by Stephens and Morris [8] was employed. This method relates the propeller dipole force F to the radiated far-field acoustic pressure P_{ff}, which is measured in previous experiments [9], through the transfer function T:

$$\log P_{ff}(f) = \log F(St) + \log T(He) \tag{15}$$

where the Strouhal number and Helmholtz number are respectively defined as

$$St = \frac{f D_p \pi}{V_{tip}} = \frac{f}{BPF} \tag{16}$$

and

$$He = \frac{fD}{c_0} \tag{17}$$

where D_p is the propeller diameter, V_{tip} is the propeller tip velocity, D is the duct diameter, and c_0 is the speed of sound.

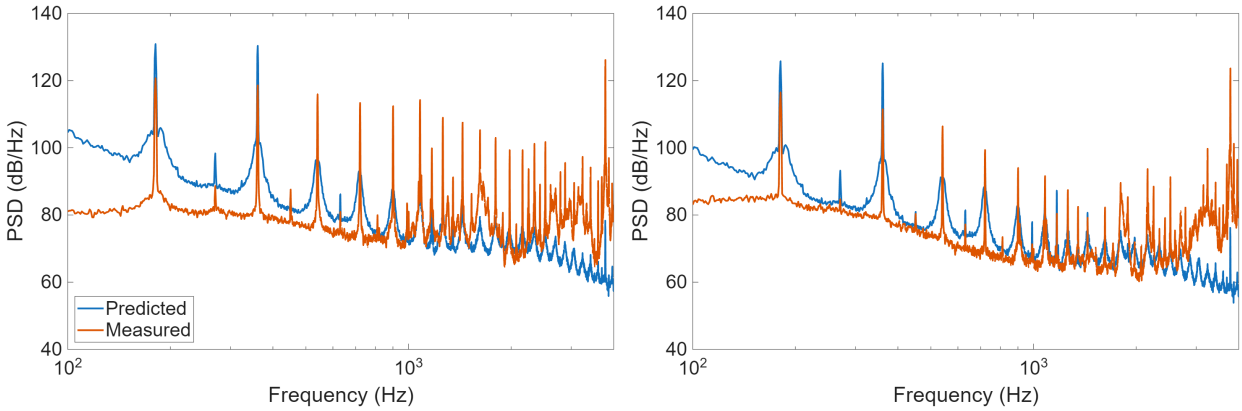
Since the acoustic spectrum is dominated by tonal components at the BPF and its harmonics, the method proposed by Tinney et al. [10] was used to quantify the energy associated with each tonal peak. The variance associated with the ith BPF harmonic at the jth microphone is defined as

$$\sigma^2_{i,j} = \int_{f_i-2\delta f}^{f_i+2\delta f} \mathrm{PSD}_j(f)\, df \tag{18}$$

and the corresponding tonal sound pressure level is calculated as

$$OASPL_{i,j} = 10\log_{10}\left(\frac{\sigma_{i,j}^2}{p_{\text{ref}}^2}\right) \tag{19}$$

where i and j denote the harmonic number and microphone index, respectively, f_i is the frequency of the ith BPF harmonic, and $\text{PSD}_j(f)$ is the power spectral density measured by remote microphone j. As an example, the measured and predicted PSDs at the fifth pressure tap (at 0.0146 m) for the propeller located at +0%L are compared in Figure 8. The corresponding tonal OASPL distributions for the first three BPF harmonics are compared with model predictions in Figure 9.



(a) Pressure tap location 5 (at 0.0146 m)

(b) Pressure tap location 8 (at -0.0292 m)

Figure 8 – Comparison of the measured and predicted ducted propeller unsteady wall pressure PSD with the propeller located at the duct center (+0%L).

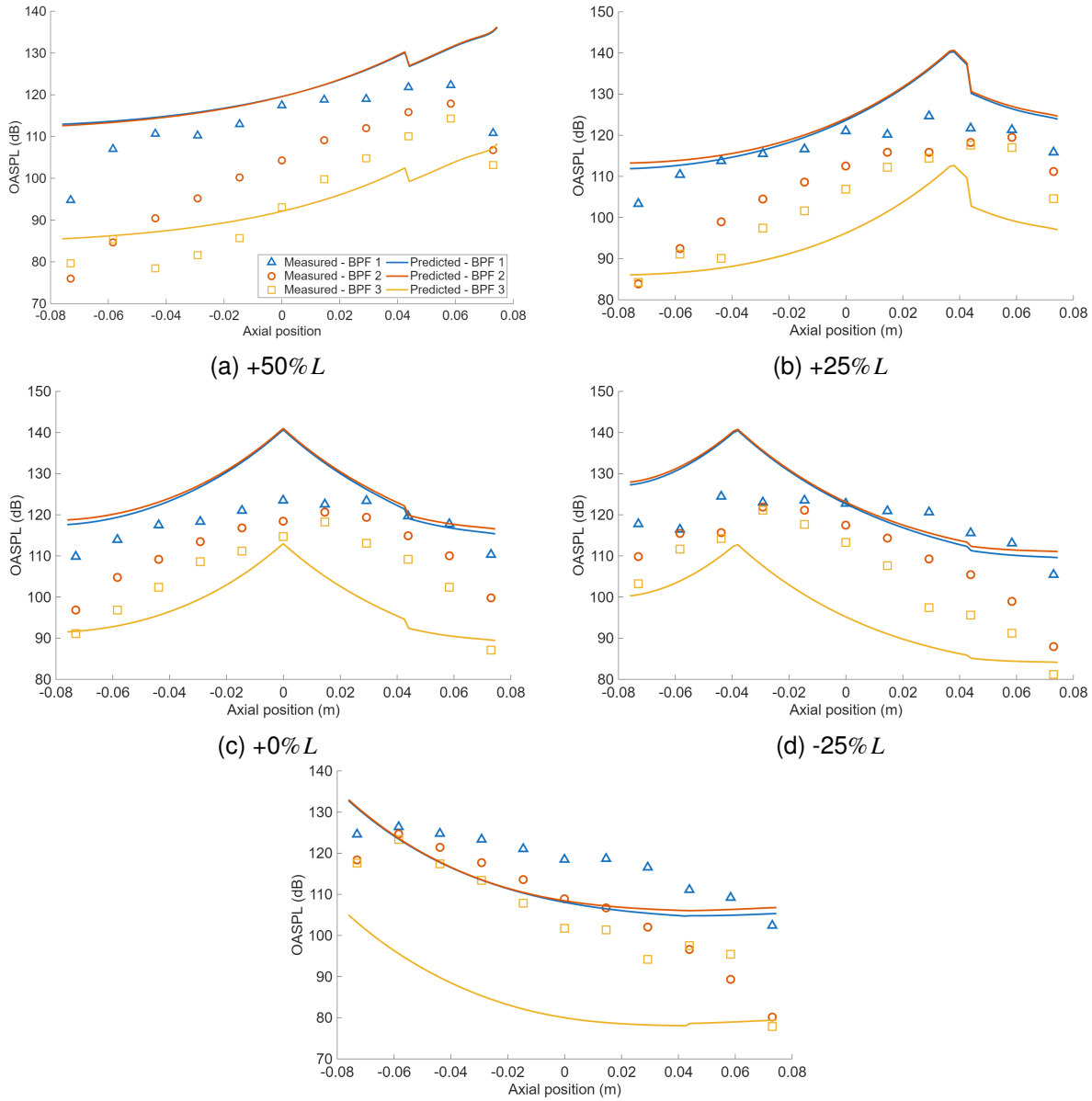
The model captures the dominant tonal peaks in the PSD spectrum reasonably well. However, discrepancies in amplitude are observed at frequencies below 1 kHz and near 3 kHz. The low-frequency discrepancy is attributed primarily to the turbulent propeller wake and its interaction with the duct boundary layer [3]. Comparison of the measured PSDs at pressure tap locations 5 and 8 shows that the downstream microphone exhibits higher amplitudes below 1 kHz, indicating the downstream convection of wake-related flow structures. The discrepancies at higher frequencies are hypothesized to be associated with tip-leakage vortex shedding and trailing-edge vortex shedding from the propeller blades.

The tonal OASPL distributions of the first three BPF harmonics exhibit similar axial trends, characterized by a primary peak located at or slightly upstream of the propeller plane, followed by a gradual decay with increasing axial distance. This behavior differs significantly from the monopole-source response, indicating a fundamentally different acoustic source mechanism. Although the model reproduces the overall axial variation, discrepancies in amplitude remain. These differences arise because the estimated dipole force spectrum $F_m(\omega)$ inherits the spectral characteristics of the far-field acoustic pressure $P(f)$, rather than the true aerodynamic loading distribution on the propeller.

For example, the prediction of the second-harmonic tonal OASPL exceeding that of the fundamental harmonic is consistent with the measured far-field acoustic spectrum of the ducted propeller. This also explains why the model provides improved agreement of the PSD at pressure tap 8 relative to pressure tap 5, as the downstream measurements are more strongly influenced by the aerodynamic effect represented in the force reconstruction process.

4. Conclusion

An experimental investigation of the unsteady wall-pressure fluctuations generated by a low-speed ducted propeller has been conducted using the remote microphone method. Measurements were performed for multiple axial propeller positions under hover flight conditions. To support interpretation of the measurements, a finite-length joint duct model was developed to account for acoustic reflections and transmission between connected duct sections of varying radius.



(a) +50%L (b) +25%L

(c) +0%L (d) -25%L

(e) -50%L

Figure 9 – Comparison of the measured and predicted ducted propeller unsteady wall pressure OASPL at BPF 1 to BPF 3 with different propeller positions.

The joint duct model was first validated using a pseudo-monopole source inside the duct. The predicted OASPL distributions agreed reasonably well with the experimental measurements and reproduced the principal axial variations of the wall-pressure field. Sensitivity analysis further demonstrated that the model was sufficiently responsive to changes in source position for the present experimental configuration. Remaining discrepancies were attributed primarily to simplifying assumptions in the reflection modeling at the duct terminations.

For the ducted propeller experiments, the measured wall-pressure spectra were dominated by tonal components at the blade-passing frequency and its harmonics. The tonal OASPL distributions exhibited consistent axial trends, with peak levels occurring near the propeller plane and decaying away from the source region. Compared with the monopole-source response, the propeller-induced wall-pressure field displayed distinctly different spatial characteristics, highlighting the importance of dipole-source mechanisms associated with aerodynamic loading.

The joint duct model captured the overall axial behaviour of the tonal wall-pressure distributions and successfully reproduced the dominant spectral peaks. However, deviations in amplitude were observed, particularly at low frequencies and around 3 kHz. The low-frequency discrepancies were as-

sociated with the interaction between the turbulent propeller wake and the duct boundary layer, while the higher-frequency deviations were likely related to tip-leakage and trailing-edge vortex shedding. Additional amplitude differences resulted from limitations in the dipole-force reconstruction method, which relied on far-field acoustic measurements rather than direct aerodynamic loading data.
Overall, the present study demonstrates the capability of the remote microphone method and the joint duct model to characterize the interior acoustic environment of ducted propellers. The findings provide improved physical understanding of the influence of the duct geometry and propeller position on unsteady wall-pressure fluctuations, and establish a foundation for future investigations of ducted propeller aeroacoustics.

5. Contact Author Email Address

Mailto: jingang.li@student.unsw.edu.au

6. Copyright Statement

The authors confirm that they, and/or their company or organization, hold copyright on all of the original material included in this paper. The authors also confirm that they have obtained permission, from the copyright holder of any third party material included in this paper, to publish it as part of their paper. The authors confirm that they give permission, or have obtained permission from the copyright holder of this paper, for the publication and distribution of this paper as part of the ICAS proceedings or as individual off-prints from the proceedings.

References

[1] Schäffer B, Pieren R, Heutschi K, Wunderli J, and Becker S. Drone noise emission characteristics and noise effects on humans—a systematic review. *International Journal of Environmental Research and Public Health*, 18, 6 2021.

[2] Zhang T and Barakos G. Review on ducted fans for compound rotorcraft. *Aeronautical Journal*, 124:941–974, 7 2020.

[3] Tomko J, Stephens D, Economon T, and Morris S. Experiments and analysis of the internal wall pressure of a ducted rotor. *Journal of Sound and Vibration*, 451:84–98, 7 2019.

[4] Moreau D, de Silva C, Kisler R, Tan J, Jiang C, Awasthi M, and Doolan C. The design and characterisation of the unsw anechoic wind tunnel. In *23rd Australasian Fluid Mechanics Conference. December, Sydney*, 2022.

[5] Awasthi M, Rowlands J, Moreau D, and Doolan C. Two-step hybrid calibration of remote microphones. *The Journal of the Acoustical Society of America*, 144(5):EL477–EL483, 11 2018.

[6] Levine H and Schvhnger J. On the radiation of sound from an unfianged circular pipe. *Phys. Rev.*, 73:383–406, 2 1948.

[7] Blackstock D. *Fundamentals of physical acoustics*. John Wiley & Sons, 2000.

[8] Stephens D and Morris S. A method for quantifying the acoustic transfer function of a ducted rotor. *Journal of Sound and Vibration*, 313:97–112, 6 2008.

[9] Li J, Yauwenas Y, Moreau D, and Doolan C. Experimental investigation on the effect of the duct length and propeller position on drone propeller noise. In *24th Australasian Fluid Mechanics Conference*, 2024.

[10] Tinney C and Sirohi J. Multirotor drone noise at static thrust. *AIAA Journal*, 56:2816–2826, 2018.